Analysis of the instability underlying electrostatic suppression of the Leidenfrost state

Arjang Shahriari,[1] Soumik Das,[2] Vaibhav Bahadur,[1] and Roger T. Bonnecaze[2,*]
[1]*Department of Mechanical Engineering, The University of Texas at Austin, Austin, Texas 78712, USA*
[2]*McKetta Department of Chemical Engineering, The University of Texas at Austin, Austin, Texas 78712, USA*
(Received 1 August 2016; revised manuscript received 11 November 2016; published 24 March 2017)

A liquid droplet on a hot solid can generate enough vapor to prevent its contact on the surface and reduce the rate of heat transfer, the so-called Leidenfrost effect. We show theoretically and experimentally that for a sufficiently high electrostatic potential on the droplet, the formation of the vapor layer is suppressed. The interplay of the destabilizing electrostatic force and stabilizing capillary force and evaporation determines the minimum or threshold voltage to suppress the Leidenfrost effect. Linear stability theory accurately predicts threshold voltages for different size droplets and varying temperatures.

DOI: 10.1103/PhysRevFluids.2.034001

I. INTRODUCTION

It is a common sight in the kitchen to observe droplets of water dancing on a hot frying pan. The evaporating liquid droplet floats above the hot surface, its weight supported by the slightly higher pressure in the thin layer of its vapor between the droplet and the surface. This simple observation, known as the Leidenfrost effect, has serious ramifications for process phenomena such as steam generation, thermal desalination, and quenching of metals [1]. Boiling heat transfer is severely degraded at high surface temperatures due to the formation of this vapor layer, which causes dryout and temperature excursions [2–6]. Numerous studies have analyzed the Leidenfrost phenomenon, with the objective of elevating the Leidenfrost temperature [3,7–10], which is the lower temperature limit of film boiling with a stable vapor layer between the droplet and the surface. Surface modification-based elevation of the Leidenfrost temperature has received the majority of research attention [11–16], with surface chemistry and texturing being the primary tools to influence the Leidenfrost state. There has been limited effort on active control and suppression of the Leidenfrost state. Celestini and Kirstetter [17] demonstrated that an electric field in the vapor gap below levitating water droplets eliminates the Leidenfrost state. Shahriari *et al.* [18] analyzed electric-field-induced suppression of the Leidenfrost state for multiple liquids at temperatures up to 550 °C and measured an order of magnitude increase in heat transfer resulting from the elimination of the vapor gap. Shahriari *et al.* [19] demonstrated that the cooling curve during quenching can be fundamentally altered by suppressing film boiling (Leidenfrost state) in favor of boiling with intimate liquid-solid contact.

Several studies have analyzed the use of electric fields to enhance boiling heat transfer [20–24]. However, all these studies are limited to electrically insulating liquids, wherein the electric field is spread out over the entire volume of the liquid. The resulting weak electric field ($\sim 0.1\,\mathrm{V}/\mu\mathrm{m}$) across the vapor gap does not enhance the heat transfer significantly. On the other hand, fluids like organic solvents (e.g., isopropanol and acetone) have much higher electrical conductivity than the conductivity of their vapor. This concentrates the electric field in the vapor gap ($\sim 10\,\mathrm{V}/\mu\mathrm{m}$), which can exert greater control on the behavior of bubbles and films and can enhance and control boiling heat transfer to a greater extent than in insulating liquids.

Here we investigate the fundamental mechanism and identify the competing forces underlying the limits of electrostatic suppression of the Leidenfrost state. We consider liquids with finite electrical conductivity, wherein the fluid remains equipotential and the entire potential difference

*rtb@che.utexas.edu

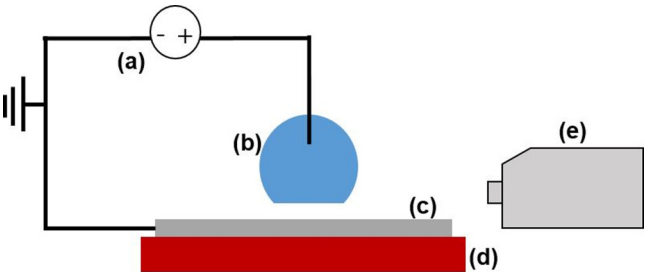

FIG. 1. Schematic of the experimental setup to visualize instabilities at the liquid-vapor interface: (a) power supply, (b) liquid droplet, (c) aluminum wafer, (d) hot plate, and (e) high-speed camera.

falls across the vapor gap. We observe and analyze the electrohydrodynamic instabilities occurring above the threshold voltage that result in a wavy liquid-vapor pattern with a characteristic wavelength. Instability analyses have been previously used in the field of boiling heat transfer [25] to estimate the critical heat flux (the heat flux beyond which stable vapor films start forming). Rayleigh-Taylor [26] and Kelvin-Helmholtz [27] instabilities are typically analyzed in such models.

There are no studies on the instabilities associated with electrostatic suppression of the Leidenfrost state, where electrostatic forces are important in addition to surface tension and evaporation-induced pressure buildup. A reasonable starting point for the analyses of instabilities underlying Leidenfrost state suppression is existing studies on instabilities of thin films during electrohydrodynamic patterning [28–32], which analyze electrostatic and surface tension forces. In this work the distinguishing feature is the presence of evaporation that adds an additional stabilizing force and leads to a critical electric field for suppression. Through a combination of linear stability analysis and experimentation, we determine the influence of material properties and surface temperature on the threshold electrical potential necessary to suppress the Leidenfrost effect. We also predict and analyze the wavelength and time constant of the fastest growing mode of disturbance at the interface.

II. EXPERIMENTS AND THEORY

Figure 1 shows a schematic of the experimental setup. Liquid droplets (5–100 μL) were dispensed on a hot surface (unpolished aluminum wafer) above the Leidenfrost temperature using a micropipette. A thin wire connected to a power source is used to set the potential of the droplet relative to the substrate, while also restricting droplet mobility. The instabilities associated with Leidenfrost state suppression were imaged from the side using a high magnification camera. The experimental protocol is similar to a previous experimental study [18] on electrical suppression of the Leidenfrost state.

Figure 2 shows the effect of an applied dc voltage on an isopropanol droplet (5 μL) on a hot surface at 400 °C. In the absence of a voltage, the droplet will remain in a stable Leidenfrost state for many minutes. As the applied voltage is increased, undulations on the liquid-vapor interface are observed. Figure 2(b) shows four or five troughs or fingers, which tend to bridge the vapor gap. The voltage corresponding to the onset of this fingering is referred to as the threshold voltage. The undulations in Fig. 2(b) are not steady-state corrugations with finite amplitude. From the visualizations the wavy interfacial instabilities are time dependent and travel due to the base flow of vapor from the center of the film to the outer perimeter or edge of the droplet. Due to limited resolution, we cannot be certain that all the undulations have the same amplitude all over the interface. Increasing the voltages results in more intimate solid-liquid contact [Fig. 2(c)] and enhanced heat transfer.

We postulate and analyze several competing forces on the perturbed interface of the droplet as the voltage approaches its threshold value. The attraction (interface destabilizing) force is due to the electrostatic attraction between the charged fingers of a disturbance on the interface and the electrically grounded surface. There are two repulsive or stabilizing effects acting on these

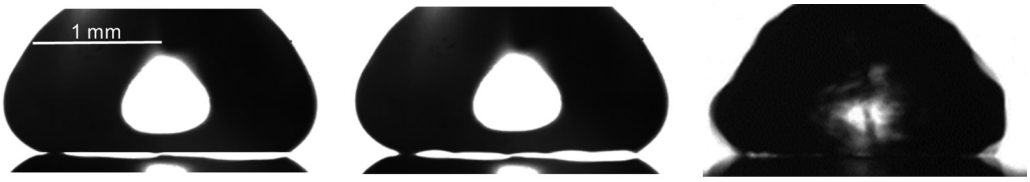

FIG. 2. A 5-μL isopropanol droplet on a hot substrate at 400 °C: (a) Leidenfrost state in the absence of a voltage, $N_C = 10.93$, $N_H = 1.15$, and $N_E = 0$; (b) wavy instability at the liquid-vapor interface under the influence of an electrical voltage of 65 V and $N_E = 2.52$; and (c) intimate liquid-solid contact at a higher voltage (130 V) and $N_E = 10.09$. Note that a reflection of the droplets can also be seen in the aluminum wafer below the vapor gap.

fingers. First, there are capillary forces that smooth out disturbances to the interface, especially the high-wave-number disturbances [32]. Second, as a finger gets closer to the interface, the rate of vaporization of the liquid increases locally and creates an additional stabilizing pressure to suppress the finger. If the applied voltage is large enough, the electrostatic force dominates and the fingers will grow and bridge the vapor gap completely, enabling liquid-solid contact. Figure 3(a) shows a high-magnification image of the liquid fingers completely bridging the gap.

We now develop an analytical model to understand these competing forces and estimate the threshold voltage for suppression of the Leidenfrost state. Consider a radially axisymmetric vapor layer of thickness $h(r,t)$ between the bottom surface of the droplet and hot surface with an electrical potential V applied across the gap [Fig. 3(b)]. Droplet evaporation results in a pressure-driven radial flow from the center to the edge (Fig. 3), generating an upward force against the weight of the droplet and setting up the Leidenfrost state. The pressure field in the vapor gap depends on the evaporation, which in turn depends on the heat transfer to the droplet. In the presence of an electric field, the bottom surface of the droplet and the hot surface act as the plates of a parallel-plate capacitor, with the liquid being electrostatically attracted to the hot surface [18]. A force balance that considers the weight of the droplet, the downward electrostatic force, and the upward pressure force on the droplet predicts the base or undisturbed vapor gap thickness h_0.

In general, the dynamics of the thickness of the vapor film, the pressure field in the gap (P), and the evaporation rate are related by the thin-film lubrication equation as [33]

$$\frac{\partial h}{\partial t} = u_{\text{vap}} + \frac{1}{12\mu r}\frac{\partial}{\partial r}\left(rh^3\frac{\partial P}{\partial r}\right), \tag{1}$$

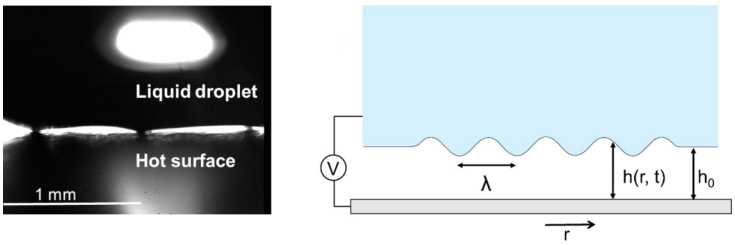

FIG. 3. Interfacial instabilities upon the application of an electrical voltage. (a) Magnified view of instabilities below a liquid droplet on a hot surface. The capillary number is $N_C = 10.93$ and the evaporation numbers are $N_H = 1.15$ and $N_E = 2.52$. (b) Schematic of the vapor gap between the bottom of the droplet and the hot solid surface. Here h_0 is the initial vapor gap thickness and λ is the wavelength of a sinusoidal disturbance to the interface.

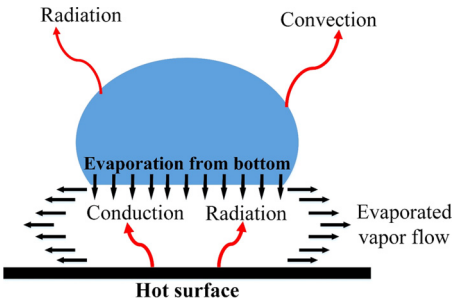

FIG. 4. Heat transfer modes involved in the Leidenfrost state.

where u_{vap} is the velocity of the vapor evaporating from the bottom of the droplet and μ is the viscosity of the vapor. The evaporation rate depends on the temperature difference between the droplet and surface, the conduction and radiative heat transfer, and the latent heat of vaporization of the liquid.

In order to estimate the normal velocity of vapor ejecting from the bottom meniscus of the droplet, all the thermal transport mechanisms must be taken into account (Fig. 4). This has been done by Shahriari *et al.* [18], and the evaporation from the bottom of the drop u_{vap} is given by

$$u_{\text{vap}} = \frac{A_b \Delta T_{\text{LF}} \left(\frac{k_v}{h} + h_r\right) - A_t h_t \Delta T_t}{A_{\text{tot}} \rho_v \Delta H_v}, \tag{2}$$

where h is the vapor gap thickness, k_v is the vapor thermal conductivity, h_r is the effective radiative heat-transfer coefficient, $\Delta T_{\text{LF}} = T_{\text{surface}} - T_{\text{drop}}$ is the Leidenfrost superheat, T_{surface} is the temperature of the hot surface, T_{drop} is the temperature of the drop, A_b is the flattened bottom surface of the droplet, A_t is the top surface of the droplet, $A_{\text{tot}} = A_b + A_t$, ΔH_v is latent heat of evaporation, ρ_v is the density of the vapor, h_t is the combined convective and radiative heat transfer from the top of the droplet, $\Delta T_t = T_{\text{drop}} - T_{\text{ambient}}$, and T_{ambient} is the ambient temperature. Estimates of the heat-transfer coefficients are found in Ref. [18]. The base value of the evaporation u^0_{vap} is given by Eq. (2) with $h = h_0$ and is constant in space.

It is assumed that the droplet volume remains constant and the droplet is isothermal. The small (millimetric) droplet size and low-heat-transfer coefficients (since the droplet is surrounded by vapor everywhere) imply the absence of significant temperature gradients within the droplet. It is noted that the electrical suppression of the Leidenfrost state is based on electrostatic attraction and does not involve the flow of large amounts of current. There is a small but finite amount of leakage current; however, the Joule heating associated with this current is negligible compared to the heat absorbed by the droplet [18]. Convection within the droplet may influence the suppression with an applied voltage, but it is neglected here. The resulting predictions, as will be shown, match experimental observations very well.

For a flat interface and radially axisymmetric flow in the absence of any disturbances, the base case satisfies

$$u^0_{\text{vap}} + \frac{1}{12\mu r} \frac{d}{dr}\left(r h_0^3 \frac{dP_0}{dr}\right) = 0 \tag{3}$$

and the base pressure distribution P_0 in the vapor gap is given by

$$P_0(r) = P_{\text{atm}} + \frac{3\mu R^2 u^0_{\text{vap}}}{h_0^3}\left(1 - \frac{r^2}{R^2}\right) + \frac{\varepsilon_v V^2}{2h_0^2}, \tag{4}$$

where P_{atm} is the ambient atmospheric pressure, R is radius of the droplet, and ε_v is the electrical permittivity of the vapor. The second term in Eq. (4) represents the pressure generated due to droplet

TABLE I. Ranges of physical parameters and dimensionless numbers N_C, N_H, and N_E.

Parameter	Range of values
Temperature	473–823 K
Vapor viscosity μ	$10^{-5} - (1.7 \times 10^{-5})$ Pa s
Evaporation rate u^0_{vap}	0.001–0.07 m/s
Droplet radius R	$10^{-3} - (3 \times 10^{-3})$ m
Surface tension γ	0.0196 N/m
Base vapor layer thickness h_0	$(2 \times 10^{-5}) - (7 \times 10^{-5})$ m
Vapor permittivity ε_v	8.904×10^{-12} F/m
Voltage V	40–80 V
$(\partial u_{\text{vap}}/\partial h)_{h_0}$	-15 to $-4000\,\text{s}^{-1}$
N_C	8–250
N_H	1–1.5
N_E	0–20

evaporation and the third term represents the electrostatic pressure upon the application of an electric voltage [18]. It is noted that van der Waals forces are negligible since the vapor gap is a few microns thick prior to complete collapse of the film above the threshold voltage.

Let us now consider a small perturbation $\eta(r,t)$ to the interface so that $h(r,t) = h_0 + \eta(r,t)$. Assuming that $|\eta|/h_0 \ll 1$ and the pressure within the droplet is constant, the pressure P in the gap is now given by [33]

$$P = P_0(r) - \gamma \frac{1}{r}\frac{\partial}{\partial r}\left(r\frac{\partial \eta}{\partial r}\right) - \frac{\varepsilon_v V^2 \eta}{h_0^3}, \tag{5}$$

where γ is liquid-vapor surface tension. The first term represents the base pressure field while the second and third terms represent, respectively, the capillary and additional electrostatic pressures resulting from the wavy interface in the presence of the perturbation. Hydrostatic effects on the pressure for a vapor film are negligible compared to the capillary and electrostatic forces.

Substitution of the pressure distribution (5) into the evolution equation of the interface (1) yields the linearized form of the evolution of the disturbance to the interface as

$$\frac{\partial \eta}{\partial t} = \left(\left.\frac{\partial u_{\text{vap}}}{\partial h}\right|_{h_0}\right)\eta - \frac{1}{12\mu r}\frac{\partial}{\partial r}\left(\frac{18\mu u^0_{\text{vap}} r^2 \eta}{h_0} + \varepsilon_v V^2 r\frac{\partial \eta}{\partial r} + \gamma r {h_0}^3 \frac{\partial}{\partial r}\left[\frac{1}{r}\frac{\partial}{\partial r}\left(r\frac{\partial \eta}{\partial r}\right)\right]\right). \tag{6}$$

Next, we assume a disturbance of the form $\eta(r,t) = \hat{\eta}(r)h_0 e^{st}$, where s is the inverse time constant of the disturbance growth. Note that, hereafter, the radial position and time are made nondimensional by scaling with R and h_0/u^0_{vap}, respectively. Substitution of this disturbance in Eq. (6) yields a fourth-order dimensionless eigenvalue equation for $\hat{\eta}(r)$ given by

$$\frac{1}{N_C}\frac{1}{r}\frac{d}{dr}\left[r\frac{d}{dr}\left(\frac{1}{r}\frac{d}{dr}r\frac{d\hat{\eta}}{dr}\right)\right] + N_E\frac{1}{r}\frac{d}{dr}\left(r\frac{d\hat{\eta}}{dr}\right) + \frac{18}{r}\frac{d(\hat{\eta}r^2)}{dr} + 12N_H\hat{\eta} = -12s\hat{\eta}, \tag{7}$$

where $N_C = \mu u^0_{\text{vap}} R^4/\gamma h_0^4$, $N_E = \varepsilon_v V^2 h_0/\mu u^0_{\text{vap}} R^2$, and $N_H = -(h_0/u^0_{\text{vap}})(\partial u_{\text{vap}}/\partial h)_{h_0}$. Here N_C and N_E are the dimensionless capillary and electroviscous numbers, which represent the relative magnitudes of viscous and interfacial forces, and electrostatic and viscous forces, respectively, and N_H represents the sensitivity of the evaporation rate to the perturbations of the initially flat interface. A list of the physical parameters and ranges of experimental conditions and the resulting ranges of dimensionless N_C, N_H, and N_E are shown in Table I.

TABLE II. Real part of the first six eigenvalues for $N_C = 28.13$ and $N_H = 1.44$ for $N_E = 0.5$, 2.33, and 5.0. These values are typical for a 5-μL isopropanol droplet at 200 °C.

Disturbance mode	$N_E = 0.5$	$N_E = 2.33$	$N_E = 5.0$
1	−31.25	0.0028	50.51
2	−81.04	−174.3	110.83
3	−368.57	−766.3	−291.1
4	−1092	−2115	−1388
5	−2614	−4536	−3507

Equation (7) is an eigenvalue problem that is solved numerically by assuming flat interfaces at both ends and no net flow at the center, namely,

$$\left.\frac{d\hat{\eta}}{dr}\right|_{r=0} = 0, \quad \left.\frac{d\hat{\eta}}{dr}\right|_{r=1} = 0, \quad \left.\frac{d}{dr}\left[\frac{1}{r}\frac{d}{dr}\left(r\frac{d\hat{\eta}}{dr}\right)\right]\right|_{r=0} = 0. \tag{8}$$

The fourth solvability condition is obtained from the zero-force contribution of the perturbed pressure, under the assumption that the weight of the droplet is constant so that

$$\int_{r=0}^{r=1} r\hat{\eta}(r)dr = 0. \tag{9}$$

Equations (7)–(9) are solved numerically using a finite-difference method to obtain eigenvalues s and the corresponding eigenfunctions. The sign of the real part of the eigenvalues determines the stability in the system for each mode of disturbance. Neutral stability corresponds to a vanishing real part of the eigenvalue for a disturbance given by its eigenfunction.

III. RESULTS

The real part of first few eigenvalues (Tables II and III) and eigenfunctions (Fig. 5) correspond to the conditions for a 5-μL isopropanol drop at 200 °C and 500 °C, at different voltages (different N_E). The imaginary part of the eigenvalues represents a traveling wave that is due to the base flow from the center of the vapor gap outward, but does not contribute to the growth or decay of the disturbance. The eigenfunctions plotted in Figs. 5(a) and 5(b) are for the conditions in the middle columns of Tables II and III, which correspond to the lowest value of N_E (lowest threshold voltage) for neutral stability, which occurs essentially for the mode 1 or mode 2 disturbance. The magnitudes of the eigenfunctions shown in Fig. 5 were normalized according to

$$\eta_{\text{norm}}(r) = \frac{\hat{\eta}(r)}{\left(\int_{r=0}^{r=1} |\hat{\eta}(r)|^2 dr\right)^{1/2}}. \tag{10}$$

TABLE III. Real part of the first six eigenvalues for $N_C = 8.76$ and $N_H = 1.11$ for $N_E = 0.5$, 2.98, and 15.0. These values are typical for a 5-μL isopropanol droplet at 500 °C.

Disturbance mode	$N_E = 0.5$	$N_E = 2.98$	$N_E = 15$
1	−36.18	0.0029	193.8
2	−282.9	−161.0	231.8
3	−1268	−1011	426.1
4	−3658	−3219	−1082
5	−8667	−7994	−4722

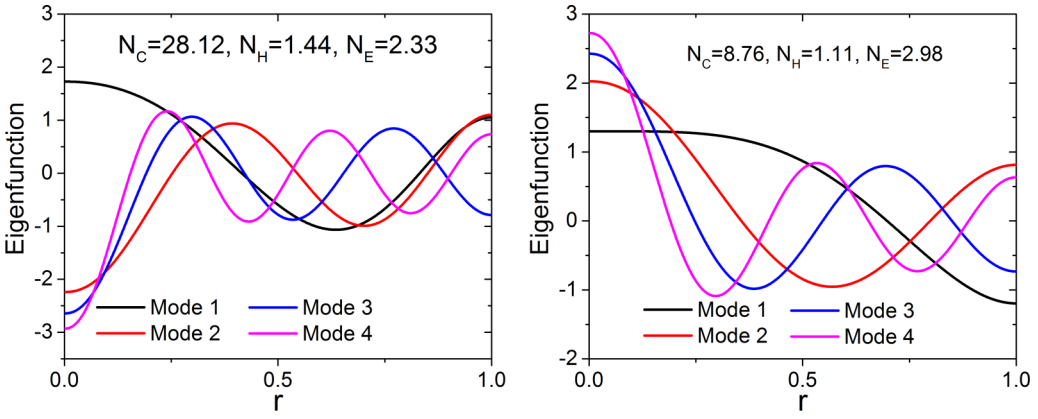

FIG. 5. First four eigenfunctions for (a) $N_C = 28.12$, $N_H = 1.44$, and $N_E = 2.33$ and (b) $N_C = 8.76$, $N_H = 1.11$, and $N_E = 2.98$.

Typical values of N_H and N_C range from 1 to 1.5 and from 8 to 200, respectively. Eigenvalues with positive real components represent an unstable system where the applied voltage is high enough to initiate Leidenfrost suppression. The neutral stability curves in which the real part of s vanishes are shown in Fig. 6.

A simple analytical solution can be obtained if the term $18r^{-1}d(\hat{\eta}r^2)/dr$ is neglected. This term is due to the advection of the base flow and only contributes to the imaginary component of the eigenvalue s and thus the traveling-wave portion of the solution. It should not significantly affect the magnitude of the real part of s, as is indeed shown to be the case below. It is informative to study this simplified problem before reviewing the full numerical solution as it clearly reveals the competing physical effects that determine the threshold voltage. Upon neglecting the aforementioned term,

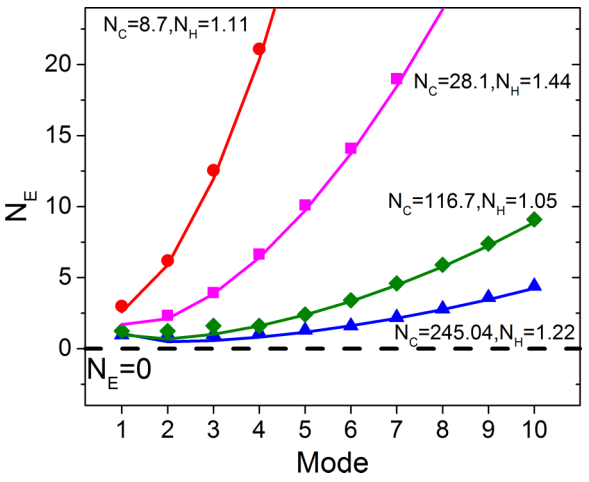

FIG. 6. Neutral stability curve of the dimensionless electrostatic force versus the mode k for varying N_C and N_H. Symbols represent the numerical solution of the neutral stability point for a given mode. The solid lines correspond to the results based on the approximate theory represented by Eq. (13).

Eq. (7) becomes

$$\frac{1}{N_C}\frac{1}{r}\frac{d}{dr}\left[r\frac{d}{dr}\left(\frac{1}{r}\frac{d}{dr}r\frac{d\hat{\eta}}{dr}\right)\right]+N_E\frac{1}{r}\frac{d}{dr}\left(r\frac{d\hat{\eta}}{dr}\right)+12N_H\hat{\eta}=-12s\hat{\eta}, \tag{11}$$

which allows a solution of the form $\hat{\eta}(r)=J_0(\lambda_n r)$, which is the zeroth-order Bessel function. Here λ_n are the roots of the equation $J_1(\lambda_n)=0$. Although there are four linearly independent solutions of Eq. (11), $J_0(\lambda_n r)$ is the only eigenfunction that satisfies Eq. (11) and the boundary conditions. This approximate solution is qualitatively close in form to the numerically computed eigenfunctions of Eq. (7). The inverse time constant for the evolution of the disturbance is then given by

$$s=\frac{u^0_{\text{vap}}}{h_0}\left(\frac{\lambda_n^2}{12}N_E-N_H-\frac{\lambda_n^4}{12N_C}\right). \tag{12}$$

Equation (12) clearly shows that the disturbances grow ($s>0$) with a sufficiently large electric field and are suppressed ($s<0$) by sufficiently large capillarity and evaporation. Note that for a vanishing electric field $N_E=0$, the vapor film is stable to all radial disturbances. The fastest growing mode occurs for $\lambda_n\approx\sqrt{\frac{1}{2}N_E N_C}$ and $s_{\max}\approx\frac{u^0_{\text{vap}}}{h_0}(\frac{1}{48}N_E^2N_C-N_H)$. (These equations are approximate since λ_n are discrete.) A neutral stability curve for $s=0$ is obtained when

$$N_E=\frac{12N_H}{\lambda_n^2}+\frac{\lambda_n^2}{N_C}. \tag{13}$$

Equation (13) estimates the nondimensional electroviscous number as a function of evaporation and nondimensional capillary forces introduced in Eq. (7). Based on this approximate model, it is seen that low-frequency disturbances are stabilized by evaporation and high-spatial-frequency disturbances are stabilized by capillary forces. The neutral stability curves for different values of N_C and N_H are plotted in Fig. 6.

Figure 6 captures the influence of various phenomena that determine the interface stability. First, it is noted that that the Leidenfrost state will be suppressed for values of N_E above the curves of neutral stability (for given capillary and evaporation numbers). For values of N_E below the neutral stability curve, stable Leidenfrost states are predicted, namely, the base state for the analysis. For the values of N_E along the neutral stability curve, there are corresponding threshold voltages V_T above which surface instabilities will grow and the Leidenfrost state will be suppressed. Additionally, the neutral stability curves and the threshold voltages decrease with increasing capillary number. Second, the interplay of competing forces is reflected in the curves. When the spatial frequency or the mode λ_n of the disturbance is high, capillary forces dominate in stabilizing the vapor layer. In this case, the neutral stability curve increases quadratically with λ_n as predicted by Eq. (13). For low-frequency disturbances evaporation becomes an additional stabilizing mechanism. Evaporation becomes the dominant mechanism at low frequencies when the capillary number is large. For medium-frequency disturbances, both capillary and evaporation effects have a comparable influence in stabilizing the disturbance.

An estimate of the first mode to go unstable can be estimated from the λ_n that minimizes Eq. (13). For this $\lambda_n\approx(12N_H N_C)^{1/4}$ and the minimum electroviscous number $N_E^{\min}\approx 4(3N_H/N_C)^{1/2}$. For typical physical parameters, $N_E^{\min}$ on the curves of neutral stability occur at low spatial frequencies, namely, the first or second mode. These first two modes correspond to two or three fingers, respectively, along the film before they become unstable. Figure 2(b) shows about four to five fingers. While Fig. 2(b) is representative of the fingers that form below the critical voltage, we cannot conclude whether the image in Fig. 2(b) is representative of the first mode that becomes unstable. The experimental setup was intended to determine the threshold voltage, but it is not at sufficient resolution to clearly identify the modes. Nonetheless, the theory accurately predicts the threshold voltage, as shown below.

Figure 7(a) depicts the variation of the threshold voltage with the volume of isopropanol droplets at two different surface temperatures. Here V_T is found to increase with increasing surface temperatures

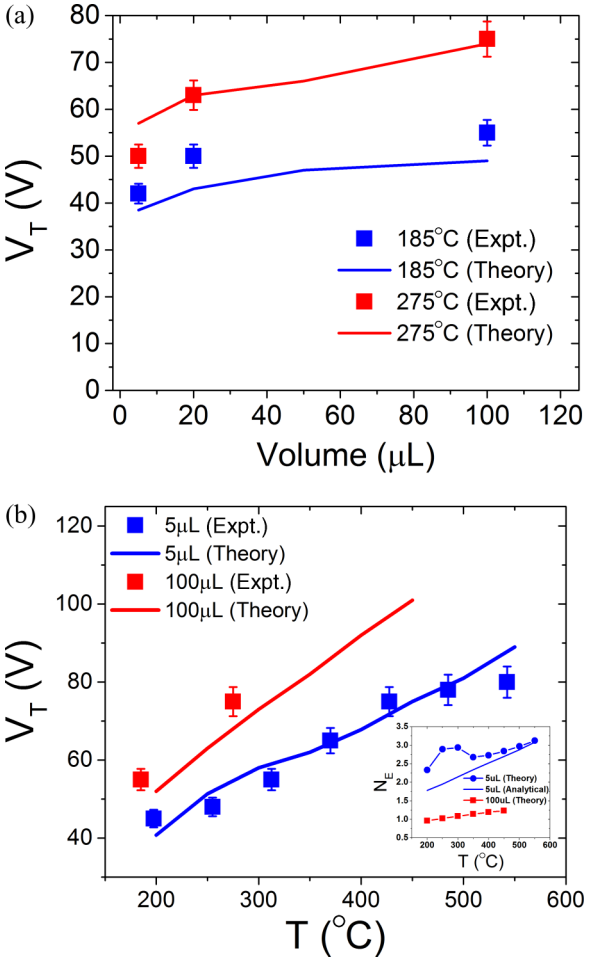

FIG. 7. Analytical and experimental measurements of the threshold voltage for suppressing the Leidenfrost state in isopropanol droplets: (a) threshold voltage as a function of droplet volume (μL) for different surface temperatures (°C) and (b) threshold voltage as a function of surface temperature for fixed droplet volume (5 and 100 μL). The reported results are the average of five or more measurements. The temperatures reported in this paper are accurate to within $\pm 2\,^{\circ}$C and the droplet volume is accurate to within $\pm 3\%$. The data here include results from Ref. [18] and additional experiments for this study. The inset in (b) shows the dimensional N_E for the experimental conditions for the two droplets and the analytic prediction for the smaller drop extracted from Eq. (13).

and droplet volumes because of the higher evaporation rates associated with these two factors. There is good agreement between the theoretical predictions and experimental observations. Figure 7(b) shows a comparison of the experimentally measured and theoretically predicted values of V_T for 5- and 100-μL isopropanol droplets at different surface temperatures. The data here include results from Ref. [18] and additional experiments for this study. The agreement between theory and experiment is very good.

Note in Fig. 7(b) that there is a slight kink in the theoretical prediction of the threshold voltage for the 5-μL droplet but not for the 100-μL droplet. The origin of this can be deduced from the inset in Fig. 7(b), which plots the N_E at neutral stability, from which the threshold voltage is derived, as a function of temperature for the two droplet sizes and the analytic prediction for the smaller drop

extracted from Eq. (13). For the smaller droplet, N_E has a small maximum, which gives rise to the kink in Fig 7(b). No such behavior is observed for the larger droplets. The analytic prediction for the smaller drop [solid blue line in the inset of Fig. 7(b)] is monotonically increasing. Thus, the origin of the kink is due to the traveling wave in the stability analysis, which was neglected in the analytic model. The traveling wave is suppressed for large N_C (high viscous forces and low capillary forces). Since $N_C \sim R^4$, viscous (capillary) forces are much higher (lower) for the larger droplet and so no kink is observed in Fig. 7(b).

IV. SUMMARY

In conclusion, the developed modeling framework shows a good match with experimental data and identifies the electroviscous number as the key determinant of Leidenfrost state suppression. This approach does not utilize any fitting factors and is based on fundamental linear stability theory and thermal-fluid transport. It is noted that this model does not predict the Leidenfrost temperature, which will depend on properties of the fluid and the surface, along with surface texture and chemistry. This model also does not consider the influence of surface texturing and chemistry on suppression, since the solid-liquid contact is very small under threshold conditions. The model can be used for other fluids used in electrowetting studies such as deionized water and low electrical conductivity organic solvents. The model cannot be used for insulating liquids such as oils or refrigerants, wherein the electric field diffuses into the droplet. While this work relates to film boiling, electric fields can also influence thermal transport in the nucleate boiling regime, which involves bubble formation. Instability analyses of vapor gaps (which in the present work are relevant to film boiling) and bubbles (nucleate boiling) under applied electric fields can together quantify the influence of electric fields on the entire boiling curve.

ACKNOWLEDGMENT

All authors contributed equally to this work.

[1] D. Quéré, Leidenfrost dynamics, Annu. Rev. Fluid Mech. **45**, 197 (2013).
[2] V. Dhir, Boiling heat transfer, Annu. Rev. Fluid Mech. **30**, 365 (1998).
[3] T. Orzechowski and S. Wciślik, Instantaneous heat transfer for large drops levitating over a hot surface, Int. J. Heat Mass Transfer **73**, 110 (2014).
[4] V. Carey, *Liquid Vapor Phase Change Phenomena*, 2nd ed. (Taylor and Francis, Washington, DC, 2007).
[5] T. Bergman, A. S. Lavine, F. P. Incropera, and D. P. Dewitt, *Fundamentals of Heat and Mass Transfer*, 7th ed. (Wiley, New York, 2011).
[6] H.-S. Roh, Heat transfer mechanisms in pool boiling, Int. J. Heat Mass Transfer **68**, 332 (2014).
[7] J. D. Bernardin and I. Mudawar, The Leidenfrost point: Experimental study and assessment of existing models, J. Heat Transfer **121**, 894 (1999).
[8] A.-L. Biance, C. Clanet, and D. Quere, Leidenfrost drops, Phys. Fluids **15**, 1632 (2003).
[9] C.-K. Huang and V. P. Carey, The effects of dissolved salt on the Leidenfrost transition, Int. J. Heat Mass Transfer **50**, 269 (2007).
[10] M. Shirota, M. A. J. van Limbeek, C. Sun, A. Prosperetti, and D. Lohse, Dynamic Leidenfrost Effect: Relevant Time and Length Scales, Phys. Rev. Lett. **116**, 064501 (2016).
[11] H. O'Hanley, C. Coyle, J. Buongiorno, T. McKrell, L.-W. Hu, M. Rubner, and R. Cohen, Separate effects of surface roughness, wettability, and porosity on the boiling critical heat flux, Appl. Phys. Lett. **103**, 024102 (2013).
[12] A. Adera, R. Raj, R. Enright, and E. N. Wang, Non-wetting droplets on hot superhydrophilic surfaces, Nat. Commun. **4**, 2518 (2013).

[13] H. M. Kwon, J. C. Bird, and K. K. Varanasi, Increasing Leidenfrost point using micro-nano hierarchical surface structures, Appl. Phys. Lett. **103**, 201601 (2013).
[14] I. U. Vakarelski, N. A. Patankar, J. O. Martson, D. Y. C. Chan, and S. T. Thoroddsen, Stabilization of Leidenfrost vapour layer by textured superhydrophobic surfaces, Nature (London) **489**, 274 (2012).
[15] R. Chen, M.-C. Lu, V. Srinivasan, Z. Wang, H. Cho, and A. Majumdar, Nanowires for enhanced boiling heat transfer, Nano Lett. **9**, 548 (2009).
[16] K.-H. Chu, R. Enright, and E. N. Wang, Structured surfaces for enhanced pool boiling heat transfer, Appl. Phys. Lett. **100**, 241603 (2012).
[17] F. Celestini and G. Kirstetter, Effect of an electric field on a Leidenfrost droplet, Soft Matter **8**, 5992 (2012).
[18] A. Shahriari, J. Wurz, and V. Bahadur, Heat transfer enhancement accompanying Leidenfrost state suppression at ultrahigh temperatures, Langmuir **30**, 12074 (2014).
[19] A. Shahriari, M. Hermes, and V. Bahadur, Electrical control and enhancement of boiling heat transfer during quenching, Appl. Phys. Lett. **108**, 091607 (2016).
[20] M. Cipriani, P. Di Marco, and W. Grassi, Effect of an externally applied electric field on pool film boiling of FC-72, Heat Transfer Eng. **25**, 3 (2004).
[21] N. Schweizer, P. Di Marco, and P. Stephan, Investigation of wall temperature and heat flux distribution during nucleate boiling in the presence of an electric field and in variable gravity, Exp. Therm. Fluid Sci. **44**, 419 (2013).
[22] D. Li, G. S. Wu, W. Wang, Y. D. Wang, D. Liu, D. C. Zhang, Y. F. Chen, G. P. Peterson, and R. Yang, Enhancing flow boiling heat transfer in microchannels for thermal management with monolithically-integrated silicon nanowires, Nano Lett. **12**, 3385 (2012).
[23] Y. C. Kweon and M. H. Kim, Experimental study on nucleate boiling enhancement and bubble dynamic behavior in saturated pool boiling using a nonuniform dc electric field, Int. J. Multiphase Flow **26**, 1351 (2000).
[24] R. Mahmoudi, K. Adamiak, and G. S. P. Castle, Flattening of boiling curves at post-CHF regime in the presence of localized electrostatic fields, Int. J. Heat Mass Transfer **68**, 203 (2014).
[25] C. H. Panzarella, S. H. Davis, and S. G. Bankoff, Nonlinear dynamics in horizontal film boiling, J. Fluid Mech. **402**, 163 (2000).
[26] B. J. Kim, J. H. Lee, and K. D. Kim, Rayleigh-Taylor instability for thin viscous gas films: Application to critical heat flux and minimum film boiling, Int. J. Heat Mass Transfer **80**, 150 (2015).
[27] B. J. Kim, J. H. Lee, and K. D. Kim, Improvements of critical heat flux models for pool boiling on horizontal surfaces using interfacial instabilities of viscous potential flows, Int. J. Heat Mass Transfer **93**, 200 (2016).
[28] E. Schaffer, T. Thurn-Albrecht, R. P. Russel, and U. Steiner, Electrically induced structure formation and pattern transfer, Nature (London) **403**, 874 (2000).
[29] P. Gambhire and R. M. Thaokar, Linear stability analysis of electrohydrodynamic instabilities at fluid interfaces in the "small feature" limit, Eur. Phys. J. E. **34**, 84 (2011).
[30] Q. Yang, B. Q. Li, and Y. Ding, *Proceedings of the ASME 2013 International Mechanical Engineering Congress and Exposition* (ASME, New York, 2013), paper IMECE2013-64471.
[31] E. O. Elele, Y. Shen, D. R. Pettit, and B. Khusid, Detection of a Dynamic Cone-Shaped Meniscus on the Surface of Fluids in Electric Fields, Phys. Rev. Lett. **114**, 054501 (2015).
[32] K. Mondal and D. Bandyopadhyay, Electro-capillary instabilities of thin leaky elastic-viscous bilayers, Phys. Fluids **26**, 122006 (2014).
[33] A. Oron, S. H. Davis, and S. G. Bankoff, Nonlinear theory of film rupture, Rev. Mod. Phys. **69**, 931 (1997).